2019

Age and Origin of Monazite Symplectite in an Iron Oxide-Apatite Deposit in the Adirondack Mountains, New York, USA: Implications for Tracking Fluid Conditions

Sean Regan

Marian Lupulescu

Michael Jercinovic

Jeffrey Chiarenzelli

Michael Williams

See next page for additional authors

Authors
Sean Regan, Marian Lupulescu, Michael Jercinovic, Jeffrey Chiarenzelli, Michael Williams, Jared Singer, and David Bailey

minerals

MDPI

Article

Age and Origin of Monazite Symplectite in an Iron Oxide-Apatite Deposit in the Adirondack Mountains, New York, USA: Implications for Tracking Fluid Conditions

Sean Regan [1,*], Marian Lupulescu [2], Michael Jercinovic [3], Jeffrey Chiarenzelli [4], Michael Williams [3], Jared Singer [5] and David Bailey [6]

1 Department of Geosciences, University of Alaska, Fairbanks, AK 99775, USA
2 New York State Museum, Albany, NY 12230, USA; Marian.Lupulescu@nysed.gov
3 Department of Geosciences, University of Massachusetts, Amherst, MA 01003, USA; mjj@geo.umass.edu (M.J.); mlw@geo.umass.edu (M.W.)
4 Department of Geology, St. Lawrence University, Canton, NY 13617, USA; jchiarenzelli@stlawu.edu
5 Earth and Environmental Sciences, Rensselaer Polytechnic Institute, Troy, NY 12180, USA; singej2@rpi.edu
6 Geosciences Department, Hamilton College, Clinton, NY 13323, USA; dbailey@hamilton.edu
* Correspondence: sregan5@alaska.edu; Tel.: +1-907-474-5386

Received: 7 December 2018; Accepted: 18 January 2019; Published: 21 January 2019

Abstract: Monazite crystals, intergrown with allanite, fluorapatite, and quartz from the Cheever Mine iron oxide-apatite (IOA-type) deposit in Essex County, New York, USA, display rare symplectite textures. Electron probe wavelength-dispersive spectrometry (WDS) mapping and major and trace element characterization of these features reveal a natural experiment in fluid-mediated monazite recrystallization. Two types of monazite with symplectite intergrowths have been recognized (Type I and II). Both types of symplectite development are associated with a decrease in HREE, Si, Ca, Th, and Y, but an increase in both La and Ce in monazite. Electron microprobe Th-U-total Pb analysis of Type I monazite with suitable ThO_2 concentrations yielded a weighted mean age of 980 ± 5.8 Ma (MSWD: 3.3), which is interpreted as the age of monazite formation and the onset of symplectite development. Both types of monazite formed during a series of reactions from fluorapatite, and possibly britholite, to produce the final assemblage of monazite, allanite, and fluorapatite. Monazite formation was likely a response to evolving fluid conditions, which favored monazite stability over fluorapatite at ca. 980 Ma, possibly a NaCl brine. A subsequent transition to a Ca-dominated fluid may have then promoted the consumption of monazite to produce another generation of allanite and fluorapatite. Our results indicate that recrystallized monazite formed during fluid-mediated processes that, over time, trended towards an increasingly pure end-member composition. Regionally, these data are consistent with a magmatic-origin followed by fluid-mediated remobilization of select phases at subsolidus conditions for the Adirondack IOA deposits.

Keywords: monazite; metasomatism; IOA-deposit; Adirondack Mountains

1. Introduction

Monazite is a commonly used geochronometer with a principal application to mid- to high-grade metamorphic rocks [1]. It is a LREE-bearing orthophosphate and participates in, and can thus monitor, many metamorphic reactions making it an invaluable tool for metamorphic petrologists [2]. It is also known to occur in lower grade rocks, in many cases associated with fluid alteration. As such, monazite may also provide a record of metasomatic events via fluid-mediated dissolution–reprecipitation [2,3],

although the literature on low-grade, fluid-related monazite is less abundant [4,5]. A better understanding of monazite associated with lower grade or retrograde terranes and fluid alteration may provide new constraints and tools for analysis of fluid–rock interaction, fault timing and basin development, and the formation of associated ore-deposits.

Iron oxide-apatite (IOA) type deposits, a subset of iron oxide copper gold (IOCG) deposits, are particularly relevant to the study of monazite in lower-grade fluid-alteration environments [6,7]. IOA deposits typically contain abundant monazite, and most recognized subvolcanic systems have associations with fluid-mediated processes, and therefore provide natural laboratories to understand monazite stability and composition in the presence of different fluids under varying geologic (pressure–temperature (P–T)) conditions. Although the extrusive El Laco IOA-type system has been interpreted as a predominately magmatic system, distinguishing the role of subsurface fluids on magma evolution persists as a major problem in discerning the complex geologic history associated with these deposits [8]. Of particular importance to this study are monazite within IOA-deposits not associated with any recognized volcanic activity in the Adirondack Mountains of New York, USA. The deposits of the Adirondack Mountains have been analyzed via zircon U-Pb methods [9–11], major and accessory phase textural analysis [10], in-situ major and trace element analysis [12], and other local isotopic analyses [13]. Here we incorporate experimental work from IOA-systems with in-situ monazite Th-U-total Pb petrochronology to better characterize the processes and timing recorded by monazite in a deeper (higher Pressure) IOA-type system.

The Adirondack Mountains in the southern Grenville Province host numerous Kiruna type iron oxide-apatite (IOA-type) deposits, all of which are associated with extensive metasomatism. Mined throughout the 1800 and 1900s for iron, tailings piles of REE-bearing fluoroapatite in the Mineville area have rejuvenated economic interest in these deposits, and are the focus of current exploration [14]. The Cheever deposit (Port Henry, NY; Figure 1) contains, at present, the highest recognized modal abundance of REE-bearing phases, and is of particular interest. The deposit consists of many different mineral types, all preserving a wide array of reaction textures [12]. Monazite is common in the Cheever deposit in association with allanite, fluorapatite, and quartz. The monazite and other REE-bearing minerals occur in a variety of textural settings including symplectite intergrowths that preserve a textural a record of a protracted alteration history. Herein we describe and present detailed phase compositions from monazite and associated fluorapatite and allanite, as well as Th-U-total Pb monazite petrochronology, of samples from the Cheever IOA-deposit as a companion contribution to other recent publications on the topic [11,12]. The textures are interpreted to have formed as part of two multi-step reaction sequences that occurred nearly simultaneously as a result of evolving fluid conditions long after ore-formation [9,11].

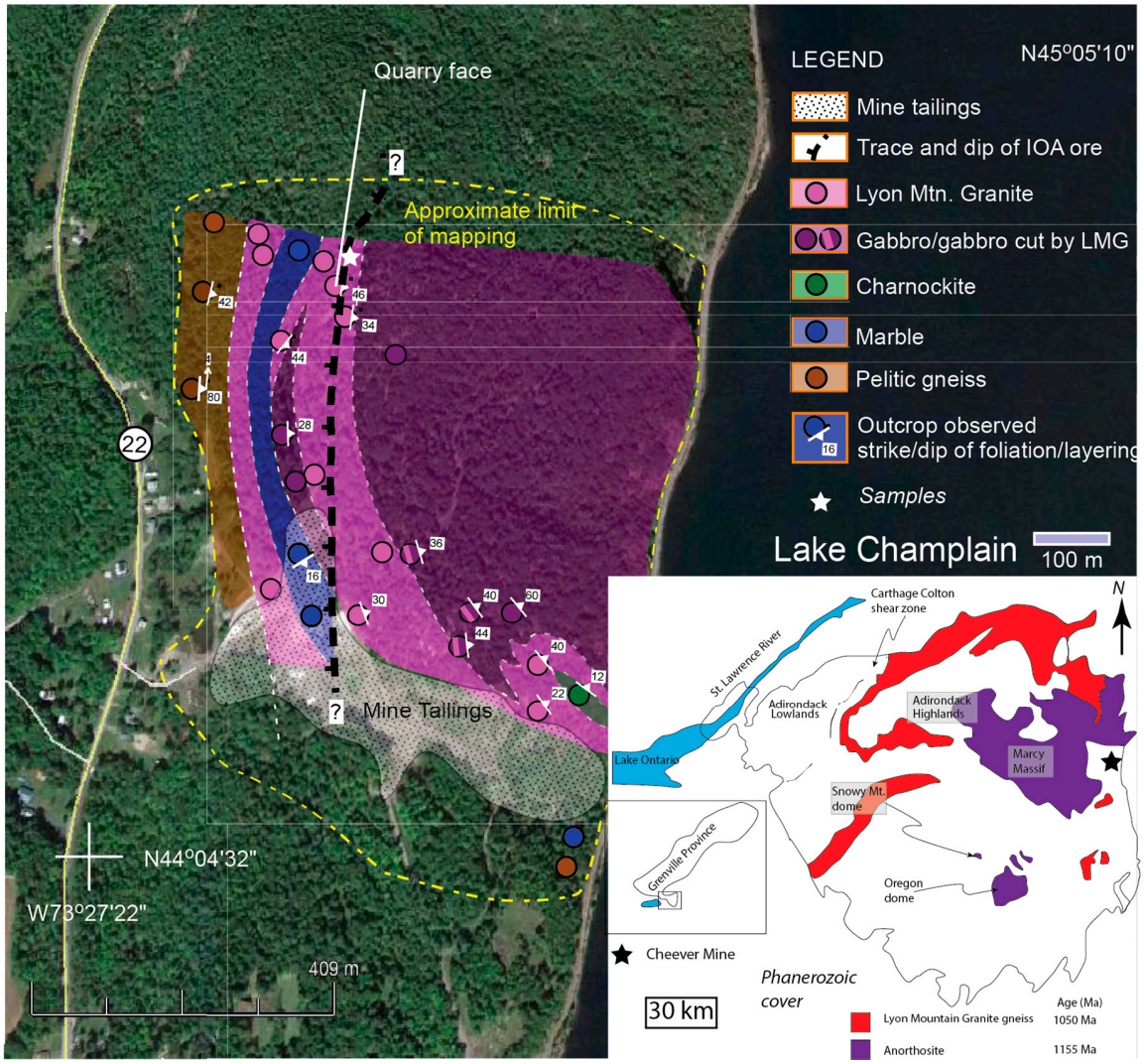

Figure 1. Detailed bedrock geology map from the Cheever Mine (modified from [11]). Inset: Simplified geologic map of the Adirondack region (modified after [11] and references therein) with the distribution of the Lyon Mountain Granite gneiss in red and inset displaying map relative to the Grenville Province and Lake Ontario. Star marks the sample. IOA: iron oxide-apatite; LMG: Lyon Mountain granite gneiss.

2. Geologic Setting

The Adirondack Highlands of northern New York form the southern extension of the contiguous Mesoproterozoic Grenville Province (Figure 1) [15]. Basement rocks have been multiply deformed and are thought to have undergone regional granulite facies metamorphism during the Shawinigan and Ottawan orogenies over 1 billion years ago [16]. The Lyon Mountain granite gneiss (LMG) was emplaced during the waning phases of granulite-facies metamorphism along the eastern and northern margins of the Adirondack Highlands, particularly where extensional structures related to orogenic collapse have been observed [17,18]. U-Pb zircon geochronology from the LMG has constrained an igneous crystallization age of ca. 1070–1030 Ma [10,17,19,20]. The LMG is typically weakly deformed to undeformed and is thought to post-date peak P–T conditions and regional deformation [14–16]. It is interpreted to have been emplaced during extensional collapse of the orogen at approximately 1070–1030 Ma [10,17–20]. Directly relevant to this study are the low-Ti, IOA deposits that are primarily hosted by the LMG.

The genesis and timing of ore formation relative to igneous crystallization of the adjacent LMG is uncertain, with models interpreting either a magmatic [11] or a later, hydrothermal [20], origin.

Valley et al. [9,20] utilized U-Pb and Hf isotopic compositions of zircon to suggest that at least some mineralization accompanied Na-fluid metasomatism as much as 40 million years after crystallization of the LMG (ca. 1015 Ma) [9]. In contrast, field relationships and ore textures indicate an igneous component to ore formation [11]. It seems likely that multiple generations of iron mineralization are present, the relative timing of which may be obscured by subsequent metasomatic alteration and iron remobilization (see Section 6). The deposits and adjacent LMG have undergone extensive sodic metasomatism that caused widespread albitization of the microperthitic LMG protolith to a quartz-albite rock [19]. Planar to folded ore bodies range in size, continuity, state of deformation [21,22], and REE abundance [22]. The Cheever IOA deposit 3.5 km north of Port Henry, NY contains the highest modal fluorapatite and REE concentrations currently known in the Adirondack Mountains, and is the focus of this study. Interestingly, IOA-type deposits of the eastern Adirondack Mountains are distinctive amongst otherwise similar IOA deposits because Adirondack examples lack volcanic equivalents and may represent deeper, mid-crustal examples of such systems.

Recent work on the textural evolution of fluorapatite, REE abundances, and zircon U-Pb systematics have been reported from the Cheever deposit [11,12]. Lupulescu et al. [12] described and reported detailed phase compositions from multiple assemblages that formed as a result of fluid-mediated processes preserved in the Cheever IOA-type deposit. The main conclusion was that coarse REE-enriched fluorapatite crystals formed within a late-magmatic setting from an iron and phosphorous-rich melt that formed via liquid-immiscibility [23]. Subsequent fluid-flow, presumably at greenschist-facies conditions lead to a secondary assemblage of low-actinide monazite, chlorite, ferro-actinolite, rutile, and hematite, among other phases discussed herein. Other late phases recognized here are allanite and another generation of fluorapatite. These interpretations [12] are consistent with zircon U-Pb geochronology from samples of both ore, quartz-albite host rock, and pegmatites associated with the Cheever mineral deposit [9–11,17,19]. Zircon U-Pb results indicate that rocks associated with the Cheever deposit formed via igneous crystallization toward the tail-end of LMG crystallization, consistent with a late-stage magmatic origin for the deposit, similar to other deposits [7].

3. Sample Description

Two samples were collected from contacts of magnetite-apatite ores with host quartz-albite rock located at the historic Cheever Mine in Port Henry, NY (Essex County; N 44°04′43.5″; W 73°27′14.3″) [24]. The ore seam is on the order of several meters thick, strikes N–S and dips moderately to the west, continuing for more than 3 km along strike. It is located near the contact between the LMG and a complex suite of mylonitic granitoids, metagabbros, and paragneisses, including marble. The ore seam is host to a variety of REE-bearing phases including fluorapatite, stillwellite, allanite, monazite, titanite, and hematite [24]. All host rocks within the vicinity of the ore have undergone some amount of sodic alteration or interaction with NaCl brines [19,20]. The main magnetite seam is exceedingly straight, and located within a small lens of LMG that delineates the contact between a ca. 1150 Ma coronitic metagabbro [25,26] east of the ore, and annealed granitic and amphibolitic tectonites intruding marble and pelitic gneisses to the west (Figure 1) [11,27]. The straight-edged nature of the Cheever deposit, and exposed discontinuities across it may indicate a fault, or tectonic control of ore emplacement; this will be addressed in detail in a future contribution. In contrast the deposits at Hammondville (20 km to the south) are folded by open, upright folds that are interpreted to be syn-kinematic with respect to LMG intrusion [10,28], consistent with a magmatic component to ore formation.

Microscopically, the contact of the Cheever ore seam with the quartz-albite host rock follows individual grain boundaries—grain truncations are lacking. The edge of the ore seam often contains a thin veneer of allanite that maintains an almost constant thickness (ca. 20 μms) between host rock and the magnetite seam consistent with a petrogenetically late-origin. The veneer of allanite is also present along many grain boundaries within the deposit, and provides a useful marker to

trace magnetite–magnetite grain boundaries. Clinopyroxene occurs locally and is restricted to the host rock and ore near the margin of the seams. No zircon has been found in-situ within the ore to evaluate textural relationships, but within the immediately adjacent quartz-albite host rock, zircon is abundant with single crystals up to 500 µm in length. The ore seam consists of over 25 modal % REE bearing phases, which vary in abundance spatially, with the remainder of the ore composed of magnetite and hematite and quartz. All REE-phases, however, contain irregular inclusions, lamellae, symplectite intergrowths, and rims of other REE-bearing phases. The most common association is coarse fluorapatite grains with thick topotaxial monazite and rims of allanite around fluorapatite [7]. Of interest to this study, however, are coarse monazite grains that preserve a variety of internal symplectite textures involving allanite, fluorapatite, and a later generation of monazite, with textures similar to those described from experimental work [29,30].

Monazite occurs primarily in two textural settings. Both contain complex reaction textures and mineral associations. The first (Type-I) includes monazite grains and inclusions in and around relatively coarse subhedral fluorapatite crystals. Most of the Type-I monazite grains contain variably developed symplectite textures within their cores, where the monazite is intergrown with an allanite-fluorapatite-quartz assemblage (Figure 2). The second setting (Type-II) involves multiphase pseudomorphs after a relatively coarse precursor phase. Type-II monazite grains are completely and complexly intergrown with allanite, (Figure 3). The pseudomorphs containing Type-II monazite are surrounded by fluorapatite and allanite rims (Figure 4).

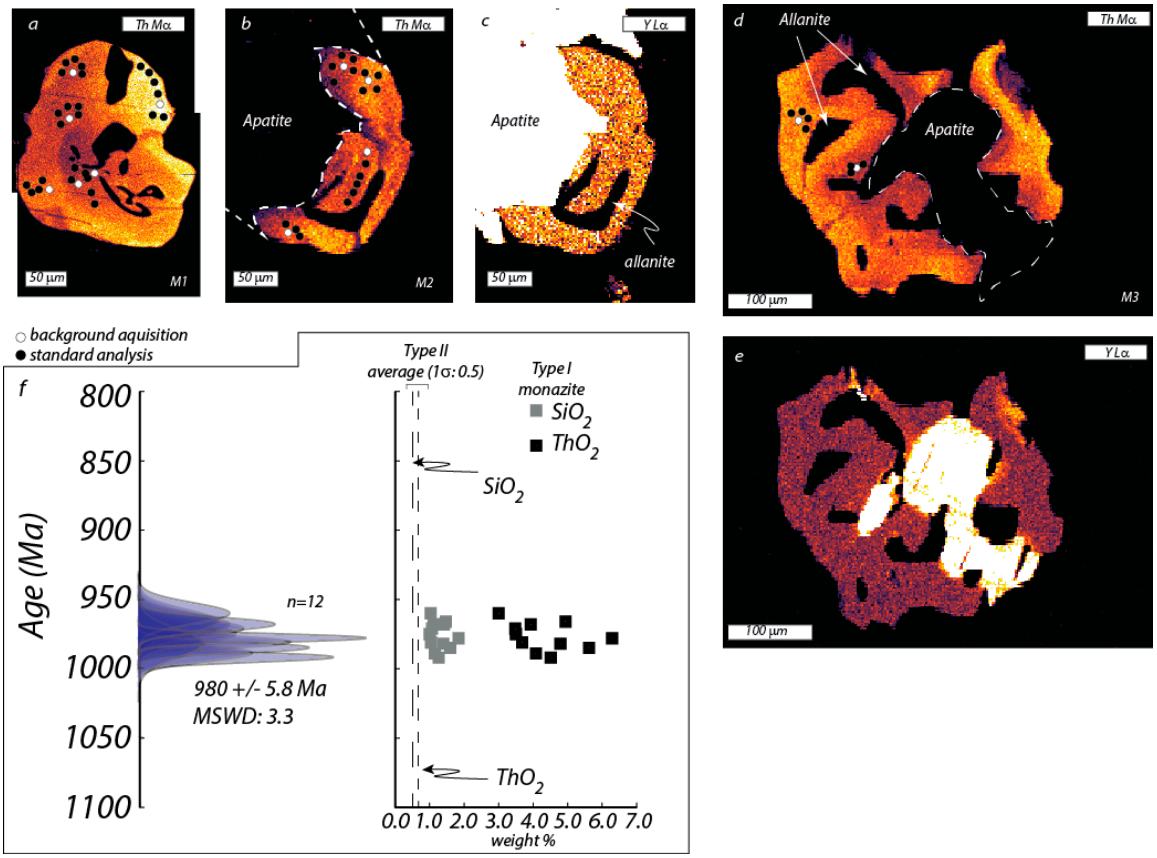

Figure 2. Wavelength-dispersive spectrometry (WDS) results for Type-I monazite. (**a**–**e**) WDS Th Mα and Y Lα beam maps of Type-I monazite; (**d**) U-Th-total Pb geochronology results plotted as Gaussian distributions with corresponding ThO_2 and SiO_2 wt. % from all type-I monazite crystals seen in histograms; dashed lines represent average composition from Type-II monazite.

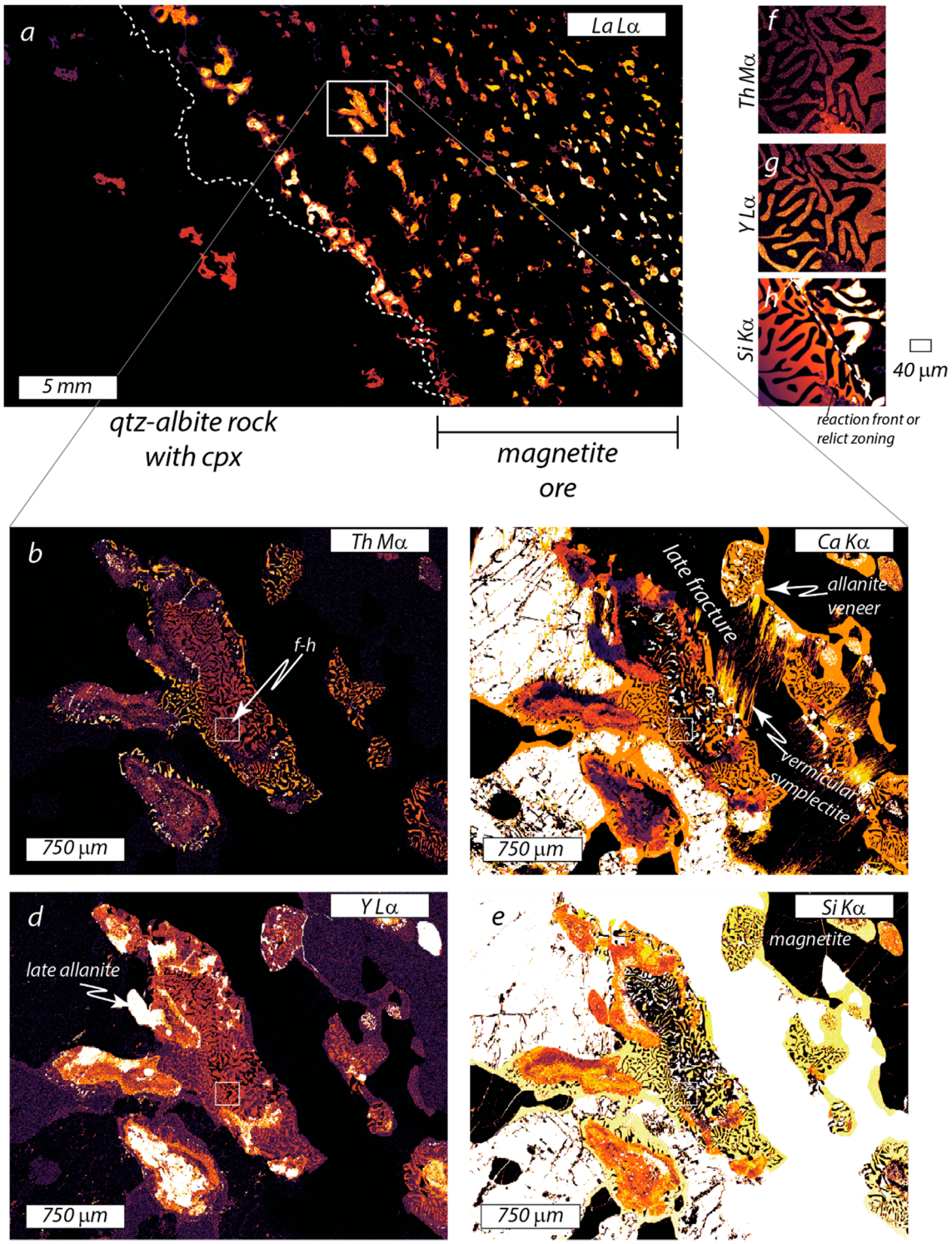

Figure 3. (**a**) Full section La Lα WDS map; (**b–e**) WDS stage maps of Type-II monazite grain; (**f–h**) WDS beam maps of monazite intergrown with allanite.

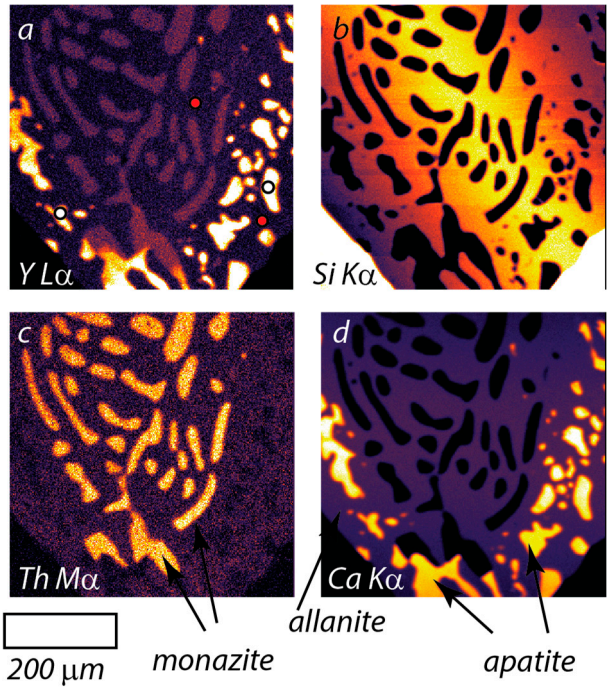

Figure 4. Close up WDS maps of Type II monazite showing relict zoning and intergrown apatite, allanite, and monazite. X-ray line labeled in lower left of each image (**a**–**d**).

4. Analytical Methods

Monazite grains were identified in polished thin sections by full thin-section compositional mapping with the Cameca SX-50 electron microprobe at the University of Massachusetts, Amherst, MA, USA. All analytical procedures were performed with a 15.0 KeV accelerating voltage. Five spectrometers were set to Mg, Y, La, Zr, and Fe with 30 μm beam size at 300 nA current, a 25 ms dwell time, and the whole thin section was scanned. Individual grains were mapped with a beam size between 2 and 4 μm, a step size set equal to the beam size, and current of 200 nA. Higher resolution images of full crystals less than 200 μm and targeted regions of large crystals were mapped by keeping the stage fixed, and rastering a focused beam across the desired region, thus achieving sub-μm resolution. All grain maps were performed with spectrometers set to Y, Si, Th, U, and Ca.

Major and trace element analyses of monazite were performed on the Cameca "Ultrachron" Electron Microprobe at the University of Massachusetts, Amherst, equipped with five spectrometers including two VLPET, two LPET, and LLIF monochromators [31]. Analyses were performed for U, Th, Pb, S, Ca, K, Sr, Si, Y, P, and REEs using a PAP method for matrix corrections [32]. Each reported analysis is an average of 4–8 individual peak analyses; background was measured on the first analytical spot [33]. Background values for U, Th, and Pb were measured using a multipoint method [33]. Standardization was performed on natural and synthetic standards [31,33]. Analyses of an internal standard, Moacyr (Age: 506 +/− 1 Ma) [34], were carried out before, after, and throughout the analytical sessions to monitor consistency.

Major and trace element analysis of allanite was performed on the Cameca SX-100 Electron Microprobe at Rensselaer Polytechnic Institute, equipped with five spectrometers including four LPET, two LLIF, and two TAP monochromators. Analyses were performed for Si, Al, Mg, Y, Fe, Mn, Ca, Sr, Th, and REEs using a PAP method for matrix corrections [32], with background determined by 2-point interpolation. Standardization was performed using natural and synthetic standards (for analytical conditions see [12]). Analyses of an in-house allanite standard were also performed.

5. Results

5.1. Type-I Monazite (Sample VGA-14)

Sample VGA-14 is dominated by quartz-albite rock (albitized microperthite granite) [9] and contains a magnetite-apatite seam approximately five mm in thickness. Type-I monazite commonly occurs as rims (several hundred microns wide) around coarse fluorapatite crystals within the host quartz-albite rock (Figure 2a–e). Symplectite intergrowths are generally restricted to the cores of monazite grains (Figure 2a–e). Symplectite intergrowths [35] consist of monazite, allanite, and fluorapatite. Twelve sets of analyses were acquired from this monazite generation to determine age and composition (Figure 2f).

Type-I monazite grains are, on average, approximately 200 μm in diameter, have bright back-scattered electron (BSE) signals, and relatively high ThO_2 contents (3.5–6.5 wt. %; see Table 1 for monazite compositions). Concentrations of Y_2O_3 are between 0.55 and 0.8 wt. % (average: 0.67; 1σ of 0.04). All samples have CaO + SiO_2 concentrations over 1.2 wt. %. A systematic decrease in Ca, Si, Th, U, and As occurs from the transition of Type-I monazite to monazite within symplectite domains, corresponding to an increase in La, Ce, and P. Owing to a high ThO_2 content, the grains belonging to this group produced robust geochronologic results, which yielded a weighted date of 980 ± 5.8 Ma (MSWD: 3.3; Figure 2f). These data are interpreted to suggest that the host monazite, and the symplectite, formed long after ore formation (ca. 1033.6 ± 2.9 Ma U-Pb zircon Cheever Mine) [11].

Fluorapatite analyses (Table 2) from the coarse crystals overgrown by Type-I monazite contain high F contents (>3.0 wt. %). Lanthanum concentrations vary, but consistently approach 5.0 wt. % in the core, i.e. farthest from the monazite rim. Cerium also varies, ranging from 2.0 to over 6.5 wt. %, again increasing toward the core of the fluorapatite grains. These data suggest that Type-I monazite may have formed at the expense of originally LREE-rich flourapatite crystals [12,36].

Table 1. Monazite major and trace element results.

	VGA-14: Type I Monazite												4UR-015: Type II Monazite						
Sample	**M1-1**	**M2-1**	**M2-2**	**M2-3**	**M2-4**	**M1-3**	**M1-4**	**M1-5**	**M1-2**	**M1-6**	**M3-1**	**M3-2**	**Core1**	**Core2**	**Core3**	**Rim1**	**Rim2**	**Core4**	**Core5**
P_2O_5	28.49	28.00	28.92	28.38	28.68	28.93	28.34	28.05	28.49	29.22	27.38	29.05	28.90	28.77	28.80	28.82	28.87	28.94	29.10
SiO_2	1.26	1.41	1.04	1.15	1.00	1.07	1.47	1.60	1.40	1.03	1.84	1.12	0.54	0.51	0.53	0.65	0.85	0.51	0.51
SO_3	0.03	0.03	0.01	0.01	0.02	0.02	0.03	0.02	0.01	0.00	0.02	0.01	0.09	0.05	0.06	0.05	0.09	0.06	0.06
ThO_2	4.51	5.33	3.68	4.08	3.50	3.48	4.94	5.62	4.79	3.00	6.29	3.93	0.41	0.51	0.46	1.03	1.47	0.46	0.45
UO_2	0.12	0.14	0.14	0.15	0.14	0.12	0.13	0.14	0.13	0.12	0.16	0.13	0.02	0.04	0.05	0.04	0.02	0.06	0.05
Y_2O_3	0.66	0.61	0.67	0.62	0.67	0.70	0.67	0.65	0.65	0.74	0.65	0.76	0.11	0.17	0.17	0.14	0.08	0.16	0.15
As_2O_3	0.16	0.09	0.18	0.14	0.13	0.14	0.12	0.11	0.18	0.13	0.13	0.13	0.26	0.21	0.36	0.23	0.26	0.42	0.30
La_2O_3	20.90	20.90	20.52	21.52	20.61	20.87	21.22	21.22	21.54	20.69	21.04	20.11	28.59	23.82	25.28	25.32	30.58	25.78	26.32
Ce_2O_3	31.54	31.52	32.81	32.27	32.79	32.79	31.68	31.38	31.85	33.23	31.04	32.55	33.21	34.87	34.78	34.33	31.31	34.81	34.56
Pr_2O_3	2.51	2.46	2.66	2.53	2.61	2.65	2.50	2.48	2.47	2.74	2.46	2.69	1.94	2.45	2.36	2.28	1.71	2.35	2.25
Nd_2O_3	8.34	8.17	8.84	8.37	8.82	8.96	8.40	8.20	8.28	9.21	8.10	9.26	5.11	6.91	6.52	6.34	4.27	6.38	6.06
Sm_2O_3	0.17	0.18	0.21	0.18	0.21	0.25	0.27	0.20	0.20	0.27	0.21	0.30	0.00	0.00	0.00	0.00	0.00	0.00	0.00
Eu_2O_3	0.07	0.06	0.05	0.06	0.06	0.10	0.11	0.09	0.09	0.08	0.08	0.12	0.00	0.00	0.00	0.00	0.00	0.00	0.00
Gd_2O_3	0.45	0.46	0.50	0.45	0.49	0.51	0.50	0.41	0.34	0.52	0.42	0.53	0.10	0.27	0.28	0.24	0.04	0.28	0.11
Tb_2O_3	0.01	0.01	0.00	0.01	0.01	0.00	0.02	0.00	0.01	0.00	0.01	0.00	0.00	0.00	0.02	0.00	0.00	0.00	0.00
Dy_2O_3	0.14	0.12	0.15	0.14	0.13	0.14	0.14	0.14	0.12	0.13	0.13	0.17	0.01	0.03	0.02	0.03	0.00	0.03	0.02
Er_2O_3	0.04	0.04	0.05	0.05	0.03	0.06	0.05	0.03	0.03	0.04	0.03	0.06	0.00	0.02	0.03	0.01	0.00	0.03	0.00
Tm_2O_3	0.07	0.04	0.06	0.06	0.06	0.07	0.04	0.04	0.03	0.05	0.04	0.08	0.03	0.04	0.05	0.02	0.00	0.06	0.04
Yb_2O_3	0.01	0.00	0.00	0.00	0.02	0.00	0.00	0.00	0.01	0.02	0.00	0.00	0.00	0.01	0.03	0.01	0.00	0.04	0.01
CaO	0.10	0.12	0.11	0.10	0.12	0.09	0.12	0.10	0.10	0.10	0.10	0.12	0.04	0.04	0.07	0.07	0.07	0.06	0.04
PbO	0.21	0.24	0.18	0.20	0.17	0.16	0.22	0.26	0.22	0.14	0.29	0.18	0.02	0.03	0.03	0.05	0.07	0.03	0.02
Total	99.85	99.99	100.76	100.41	100.26	101.09	100.97	100.72	100.93	101.43	100.37	101.33	99.41	98.75	99.97	99.69	99.72	100.53	100.07
Age (Ma)	992	968	981	989	975	971	966	985	982	960	978	968				947	994		
2σ	7	15	9	12	14	13	17	8	21	15	7	10				18	18		

5.2. Type-II Monazite (Sample 4UR-015)

Type-II monazite occurs exclusively within the magnetite seam and consists of complex intergrowths of monazite, allanite, fluorapatite, and quartz (Figure 3a). There are several discrete fractures throughout the seam that contain vermicular symplectites of allanite and several other fine-grained silicates, including epidote, chlorite, allanite, and talc. These fractures appear to have been conduits for late stage fluids. Nearly all monazite is complexly intergrown with other phases, and is thus interpreted to have formed from a precursor phase [35]. Individual monazite lamallae are 3 to 100 μm wide (Figure 3f–h). As discussed below, the Type-II intergrowths are interpreted to be pseudomorphs of pre-existing crystals that ranged from approximately 0.5 to 4.0 mm in length (Figure 3b–e). Several of the Type-II monazite bearing pseudomorphs themselves have rims (up to 50 um) of intergrown allanite and fluorapatite without any monazite (Figure 4). Seven sets of analyses were performed to characterize the Type-II monazite compositions.

Type-II monazite is bright in back-scattered electron images relative to the associated allanite, apatite, and magnetite. However, in contrast to the Type-I monazite, the Type II monazite contain less than 1.4 wt. % ThO_2 (average UO_2 + ThO_2 = 0.72; 1σ of 0.40), less than 0.18 wt. % Y_2O_3 (average = 0.14; 1σ of 0.03), and a small range of SiO_2 + CaO, with an average of 0.64 wt. % (1σ of 0.14). Due to low total actinide concentrations, Pb concentrations were near detection limit for five out of seven analyses, and thus total Pb ages could not be reliably calculated. Two sets of analyses yielded ThO_2 just over 1.0 wt. % and U-Th-total Pb ages of 947 ± 18 Ma and 994 ± 18 Ma, the older of which is within error of the weighted mean calculated from the Type-I monazite. Given the results and textures preserved in the Type-I monazite, we conclude that ca. 980 Ma is a reasonable constraint on monazite formation and initial symplectite development, but no constraints on the lower age limit were acquired.

Table 2. Major and Trace element results from allanite and fluorapatite.

Sample	FAp-1	FAp-2	FAp-3	Aln-1	Aln-2	Aln-3	Aln-4
P	16.4	13.81	13.39	na	na	na	na
Si	1.21	2.31	2.42	13.07	13.57	13.32	13.17
Th	na	na	na	0.06	0.01	0.04	bd
Y	1.49	2.74	0.89	0.13	0.11	0.10	0.09
La	0.29	0.58	4.04	9.07	8.00	10.25	9.18
Ce	1.23	2.55	6.65	11.14	11.80	10.83	11.40
Pr	0.27	0.61	1.03	1.81	1.89	2.01	1.91
Nd	1.42	2.68	2.27	1.79	2.38	1.50	1.76
Sm	0.19	0.36	0.16	0.03	0.02	Bd	bd
Gd	0.37	0.64	0.14	bd	bd	bd	bd
Dy	0.24	0.45	0.09	bd	bd	bd	bd
Fe	0.20	0.36	0.33	16.41	16.46	17.89	18.07
Al	na	na	na	4.70	4.79	3.81	3.77
Na	0.02	0.04	0.16	na	na	na	na
Mg	na	na	na	0.35	0.34	0.31	0.31
Ca	36.05	32.77	29.33	6.58	6.47	6.34	6.36
Mn	bd	bd	0.02	0.05	0.04	0.05	0.04
Cl	0.29	0.37	0.12	na	na	na	na
F	2.53	2.34	3.44	na	na	na	na
Total	100.30	98.36	100.76	99.29	99.26	98.93	98.54

na: not analyzed; bd: below detection.

Representative analyses of allanite and fluorapatite from these pseudomorphs are presented in Table 2. Compositions and variability of other REE bearing phases and coarse fluorapatite crystals have been discussed in a separate contribution [12]. Allanite grains adjacent to Type II monazite have consistent Si (13.17–13.55 wt. %), Y (~0.1 wt. %), Ca (6.4 wt. %), Ce, Pr, and Th concentrations, but Al, Fe, La, and Nd have greater variability. Allanite exposed along the rim, locally intergrown with fluorapatite, also varies considerably in composition, but typically has slightly less Fe and Nd,

but more La, than allanite associated with Type II monazite within the interior of the pseudomorph (Figure 4).

All fluorapatite grains analyzed in this study contain over 2.0 wt. % F. Analyses were taken from the rims of symplectites, which are intergrown with allanite (Figure 4). There are two distinct populations of fluorapatite within the rim symplectites (Figure 5a–d). The population with slightly higher F contents contains a higher concentration of pure end-member elements (Ca and P), and lower concentrations of REE and Y. High-F fluorapatite grains contain significantly less Cl (~0.29 wt. %) than other fluorapatites, which contain ~0.37 wt. % Cl. Given the compositional variability, even within one small domain within the symplectite, we interpret an initially heterogeneous, or zoned parent mineral (see below), that led to the compositionally diverse phases within the pseudomorph.

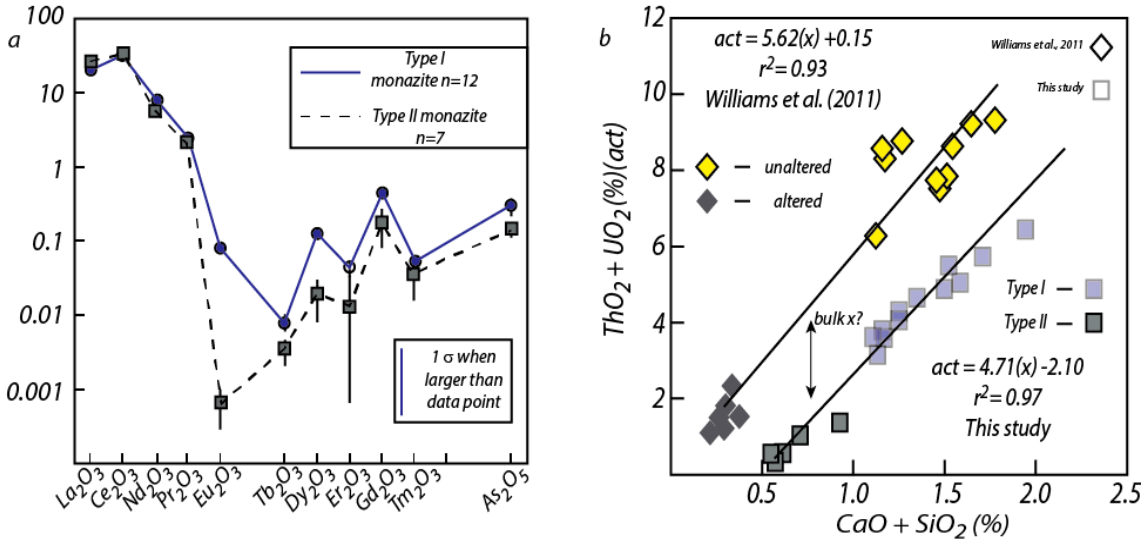

Figure 5. (**a**) REE concentrations of averaged Type I and Type II monazite in this study (*y*-axis in wt. %); (**b**) Actinides vs. CaO + SiO_2 in both Type I and Type II monazite compared to experimental results in [3].

6. Discussion

6.1. Compositional Variability and Timing

Two populations of monazite have been identified in and adjacent to IOA "ore" samples from the Cheever mine. Type I monazite has higher ThO_2, CaO + SiO_2 (cheralite), and Y_2O_3 concentrations relative to Type II monazite. However, near symplectite intergrowths within Type I grains, ThO_2, CaO, SiO_2, and Y_2O_3 all decrease, suggesting that these components are not favored in the monazite crystal during symplectite formation and monazite recrystallization. U-Th-total Pb geochronology of these grains yield no resolvable age differences, which suggests that both Type I monazite growth and subsequent symplectite formation occurred around 980 Ma. Type II monazite has a different composition and textural evolution than does Type I monazite, a consequence of forming within a different local compositional environment in the host ore. Two sets of U-Th-total Pb analyses of Type II monazite grains suggest formation at approximately the same time as the Type I monazite and subsequent symplectite development in Type I monazite.

Type I monazite commonly forms rims on fluorapatite, has higher Ca + Si and actinide concentrations, and lower La, Ce, and P than Type II monazite. Fluorapatite cores contain a heterogeneous distribution of LREEs, which decrease toward rims and topotaxial inclusions of Type I monazite. This is similar to results obtained in experimental work by [29,30,36–42], and to another natural occurrence in southwestern Germany [6,42]. Qualitatively, there is far less allanite and more fluorapatite associated with Type I than Type II monazite. We interpret Type I monazite to have formed from the fluid-mediated dissolution–reprecipitation of REE-rich fluorapatite [12,29,30,36]. Symplectite

textures within Type I monazite consist primarily of allanite and fluorapatite, and are interpreted to represent a monazite consuming reaction.

The compositions of allanite and fluorapatite intergrown with Type II monazite provide a glimpse into the reaction history recorded in the Cheever IOA-type deposit. Fluorapatite is present as beads within allanite, and is associated with the rims of the Type II monazite-allanite-bearing pseudomorph. Both fluorapatite and allanite are compositionally variable, each having distinct major and trace element compositions, even within a single textural population. However, variability is reproducible. For instance, within the rim of a symplectite, from outside the Type-II monazite zone (Figure 4), there are two distinct and reproducible populations of fluorapatite, which vary by over 0.5 wt. % in Y, Si and F (Table 2).

6.2. Reaction Constraints

Recent experimental work [37] provides potential insight into the reactions observed in this study. Experiments were performed at a wide range of temperatures (300, 400, 500, and 600 °C), well within the temperature constraints of ore formation within the eastern Adirondack Mountains, but at substantially lower pressures (100 MPa). These data paired with existing, higher pressure experiments (450–600 MPa) provide constraints and predictable responses to varying fluid composition in IOA systems [29,30]. Different proportions of fluorapatite and monazite were exposed to an $H_2O + Na_2Si_2O_5$ solution. Alteration and recrystallization in both phases was widespread in experiments at 500 and 600 °C, and resulted in the formation of britholite ($(Ce,Ca,Th,La,Nd)_5(SiO_4,PO_4)_3(OH,F)$) and vitusite [$Na_3(Ce,La,Nd)(PO_4)_2$] [37]. Experiments at 600 °C produced a symplectite at the reaction front consisting of intergrown vitusite and britholite, which both formed at the expense of monazite.

Metasomatism is commonly invoked for the mobilization and concentration of IOA-type deposits [7]. Rocks in proximity to IOA-type deposits of the Adirondack Mountains contain evidence for interacting with sodic fluids that contained elevated $fO2$ [20]. Alkali-bearing fluids have been experimentally demonstrated to be catalysts for dissolution–reprecipitation reactions in monazite [7,38,41,42]. Based on the relatively high Cl concentrations in the Fluorapatite, NaCl brines may have been a predominant fluid in the Cheever system. In general, alkali-fluids cause REE mobility, which catalyzes further reequilibration and recrystallization [37]. Geochronologic results suggest that monazite and symplectite formation occurred long after albitization and ore formation, interpreted as syn-magmatic with the LMG~1050 Ma [10–12]. Textures and mineral assemblages resemble experimental results of fluid-mediated dissolution–reprecipitation reactions [36–42]. Therefore, the reactions described here are interpreted to have formed in an open system, which likely involved alkali-fluids that facilitated the mm-scale mobility of REEs, Si, P, Ca, Na, and Al, among many other immobile ions, and possibly externally derived soluble species.

In the context of experimental work presented in [37], we interpret the Type II monazite to have formed via fluid mediated dissolution–reprecipitation of britholite. The initial phase hosting Type II monazite would have to contain both SiO_2 and P_2O_5 as major anions (Figure 6), consistent with compositions presented in [37] (SiO_2 concentrations of 12.49 to 24.33 wt. %, and P_2O_5 concentrations ranging from 9.73 to 15.09 wt. %). Variations in phase composition paired with proportionality disparities (variations in monazite/allanite proportion) make rigorous reintegration of complexly intergrown phases difficult (Figure 3h). However, simple averaging of end member compositions by applying a single monazite composition for all monazite and a single allanite composition produces chemistry similar to britholite produced experimentally [34]. In essence, the observed reaction is the reverse of those described in their experimental work [34], and interpreted to be a retrograde reaction. The rims of the pseudomorph consist of a symplectite of fluorapatite + allanite, with no observable monazite. This could be the result of Type II monazite and allanite reacting to produce an assemblage of fluorapatite and allanite, or the result of initial compositional variability in the original britholite crystal. The former is favored owing to geometric continuity of monazite into fluorapatite.

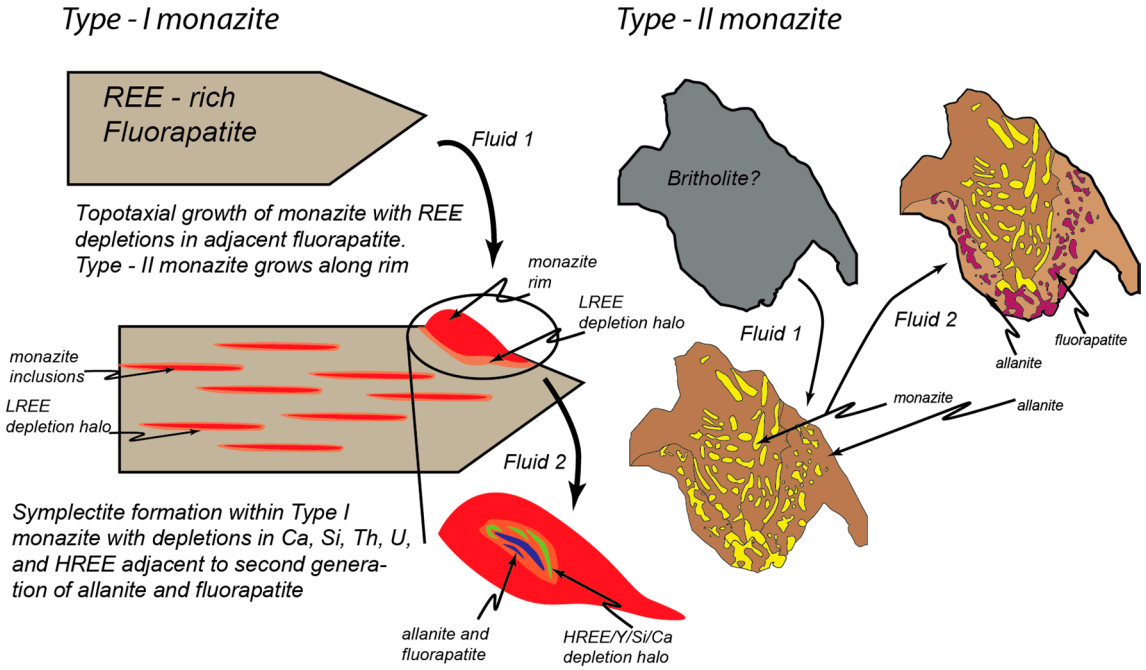

Figure 6. Schematic drawing proposing the reaction history and textural evolution of monazite-allanite-fluorapatite assemblages discussed in this this study.

These observations suggest that monazite described above formed as a result of a multi-step, fluid-mediated, reaction history beginning with the assemblage of REE-rich fluorapatite and possibly, britholite ultimately producing REE-poor fluoroapatite, allanite, and monazite. Britholite initially reacted to form Type II monazite and allanite, which then locally reacted to an allanite + fluorapatite assemblage along the rims. Fluorapatite reacted to Type I monazite, which then began to recrystallize to an allanite + flourapatite assemblage, preserved in the core of Type I monazite. These reactions are similar from those described [43], but without epidote (present in thin section but not immediately involved in reactions). Similar to interpretations made in [43], the monazite-out reaction is limited to the rims of britholite pseudomorphs, suggesting that these reactions likely document continued retrogression. Timing constraints suggest that these reactions occurred long after ore formation (1040–1020 Ma) [9,11] indicating that fluid–rock interaction may have been long-lived or episodic over a long period of time (as much as 60 my). These constraints provide strong evidence that IOA deposits of the Adirondack Mountains formed as the result of both magmatic and externally-derived fluids, and that the latter, continued for tens of millions of years after crystallization and were responsible for ore remobilization and recrystallization.

6.3. A Record of Evolving Fluid Conditions

Monazite-allanite-fluorapatite stability relationships have been investigated in a number of experimental studies [6,7,29,30,36–43]. These studies indicate that pressure–temperature (P–T) conditions are of minor importance to phase stability, particularly in the presence of fluids, where fluid composition is the fundamental control on stable assemblages [29,36]. Therefore, the observed textural evolution, and specifically the transient phase of monazite stability, was likely a result of variations in fluid composition over time.

Based on the geochronologic data, both Type I and Type II monazite formed at approximately the same time, but at the expense of different parent minerals (fluorapatite and britholite, respectively). Both Type I and Type II monazite preserve later assemblages that indicate fluorapatite and allanite formed at the expense of monazite +/− allanite. Therefore, monazite became stable, and over the course of tens of millions of years, became unstable again. Based on experimental work presented in [29,37], it seems likely that minor variations in metasomatic fluid-composition could explain these

reactions. Na-dominated fluids may have originally promoted the formation of monazite at the expense of fluorapatite and britholite. Following this, an increase in Ca concentration of the fluid stabilized allanite and fluorapatite, and promoted the consumption of monazite, and are similar to reactions described in [43].

Monazite crystals within and adjacent to ore samples from the historic Cheever Mine in the eastern Adirondack Highlands preserve evidence for varying degrees of fluid-mediated recrystallization well below the closure temperature for Th and Pb diffusion in monazite [44,45]. Experimental work presented in [39], and major and trace element microanalysis presented in [3], show that fluid-mediated dissolution–reprecipitation of monazite can occur at modest temperatures (450 °C), and essentially "purifies" the crystal, including efficient removal of radiogenic Pb, thus resetting the apparent age. Altered domains contain less Ca + Si and total actinides compared to unaltered domains. Ca + Si plotted against U + Th from the experimental work form a line with a slope near 5.6 (Figure 5b). Results plotted from this study show a wider spread in compositions, but along a line of similar slope (slope of 4.7), which includes Type I and II monazite compositions. The relationship results from the dependence that huttonite and cheralite components have on the ThO_2 content of the monazite, and is consistent with compositional data from experiments on monazite susceptibility to fluid-mediated dissolution–reprecipitation.

These results provide further evidence, from a natural occurrence, that fluid-related recrystallization of monazite, well below the closure temperature for Th and Pb diffusion, trends towards end-member Ce-La monazite. This conclusion confirms similar assertions determined from experimental work [3,4,36–39,42] and from natural examples presented in [36,40–42,46,47]. Furthermore, the data demonstrate that substitution of cheralite and huttonite components are the primary mechanisms for incorporating ThO_2 into monazite [1], and that higher grade crystals may be more radiogenic due to higher concentrations of these solid-solution components. This is also consistent with low actinide, and low cheralite and huttonite components reported from diagenetic monazite in the Cambrian Potsdam Sandstone in New York, USA [48]. These data further demonstrate that REEs and monazite are mobile under modest temperatures and appropriate fluid compositions [38]. It follows that the interpretation of monazite geochronology needs to be coupled with a systematic understanding of compositional variability, phase associations, and recrystallization processes within each petrologic system to better recognize and identify monazite affected by fluid-mediated reactions.

Author Contributions: Conceptualization: S.R., M.L., J.C., and D.B.; Methodology: M.J., M.W. and J.S.

Funding: This research was funded by the U.S. Geological Survey (USGS) National Cooperative Geologic Mapping Program (NCGMP), the USGS Pathways Internship Program, and the New York State Museum.

Acknowledgments: Ryan Taylor and Greg Walsh are acknowledged for revisions during internal USGS review. The Real family is acknowledged for access to the Cheever deposit. Paul and Mary-Lloyd Borroughs are acknowledged for constant hospitality and logistical support during work in the eastern Adirondack Mountains.

Conflicts of Interest: The authors declare no conflict of interest.

References

1. Spear, F.S.; Pyle, J.M. Apatite, Monazite, and Xenotime in Metamorphic Rocks. *Rev. Mineral. Geochem.* **2002**, *48*, 293–335. [CrossRef]
2. Williams, M.L.; Jercinovic, M.J.; Hetherington, C.J. Microprobe Monazite Geochronology: Understanding Geologic Processes by Integrating Composition and Chronology. *Annu. Rev. Earth Planet. Sci.* **2007**, *35*, 137–175. [CrossRef]
3. Williams, M.; Jercinovic, M.; Harlov, D.; Budzyń, B.; Hetherington, C. Resetting monazite ages during fluid-related alteration. *Chem. Geol.* **2011**, *283*, 218–225. [CrossRef]
4. Grand'Homme, A.; Janots, E.; Seydoux-Guillaume, A.-M.; Guillaume, D.; Bosse, V.; Magnin, V. Partial resetting of the U-Th-Pb systems in experimentally altered monazite: Nanoscale evidence of incomplete replacement. *Geology* **2016**, *44*, 431–434. [CrossRef]

5. Zi, J.-W.; Rasmussen, B.; Muhling, J.R.; Fletcher, I.R.; Thorne, A.M.; Johnson, S.P.; Cutten, H.N.; Dunkley, D.J.; Korhonen, F.J. In situ U–Pb geochronology of xenotime and monazite from the Abra polymetallic deposit in the Capricorn Orogen, Australia: Dating hydrothermal mineralization and fluid flow in a long-lived crustal structure. *Precambrian Res.* **2015**, *260*, 91–112. [CrossRef]
6. Harlov, D.E. Apatite: A fingerprint of metasomatic processes. *Elements* **2015**, *11*, 171–176. [CrossRef]
7. Harlov, D.E.; Persson-Nilsson, K.; Jonsson, E.; Majka, J.; Högdahl, K. Fluorapatite-monazite-allanite relations in the Grängesberg apatite-iron oxide ore district, Bergslagen, Sweden. *Am. Mineral.* **2016**, *101*, 1769–1782.
8. Bilenker, L.D.; Simon, A.C.; Reich, M.; Lundstrom, C.C.; Gajos, N.; Bindeman, I.; Barra, F.; Munizaga, R. Fe–O stable isotope pairs elucidate a high-temperature origin of Chilean iron oxide-apatite deposits. *Geochim. Cosmochim. Acta* **2016**, *177*, 94–104. [CrossRef]
9. Valley, P.M.; Hanchar, J.M.; Whitehouse, M. New insights on the evolution of the Lyon Mountain Granite and associated Kiruna-type magnetite-apatite deposits, Adirondack Mountains, New York State. *Geosphere* **2011**, *7*, 357–389. [CrossRef]
10. Chiarenzelli, J.; Selleck, B.; Lupulescu, M.; Regan, S.; Bickford, M.E.; Valley, P.; McLelland, J. Lyon Mountain Ferroan Leucogranite Suite: Response to Collision, Thickened Crust, and Extension in the Core of the Grenville Orogen. *GSA Bull.* **2017**, *129*, 1472–1488.
11. Chiarenzelli, J.R.; Lupulescu, M.V.; Regan, S.P.; Singer, J.W. Age and Origin of the Mesoproterozoic Iron Oxide-Apatite Mineralization, Cheever Mine, Eastern Adirondacks, NY. *Geosciences* **2018**, *8*, 345. [CrossRef]
12. Lupulescu, M.V.; Hughes, J.M.; Chiarenzelli, J.R.; Bailey, D.G. Texture, Crystal Structure, and Composition of Fluorapatites From Iron Oxide-Apatite (Ioa) Deposits, Eastern Adirondack Mountains, New York. *Can. Mineral.* **2017**, *55*, 399–417. [CrossRef]
13. Chew, D.M.; Sylvester, P.J.; Tubrett, M.N. U–Pb and Th–Pb dating of apatite by LA-ICPMS. *Chem. Geol.* **2011**, *280*, 200–216. [CrossRef]
14. Long, K.R.; Van Gosen, B.S.; Foley, N.K.; Cordier, D. *The Principal Rare Earth Element Deposits of The United States—A Summary of Domestic Deposits and a Global Perspective*; U.S. Geological Survey Scientific Investigations Report; USGS Western Mineral and Environmental Resources Science Center: North Gemini Drive Flagstaff, AZ, USA, 2010; 96p.
15. McLelland, J.M.; Selleck, B.W.; Bickford, M.E. Review of the Proterozoic evolution of the Grenville Province, its Adirondack outlier, and the Mesoproterozoic inliers of the Appalachians. In *From Rodinia to Pangea: The Lithotectonic Record of the Appalachian Region: Geological Society of America Memoir*; Tollo, R.P., Bartholomew, M.J., Hibbard, J.P., Karabinos, P.M., Eds.; Geological Society of America: Boulder, CO, USA, 2010; Volume 206, pp. 1–29.
16. Rivers, T. Assembly and preservation of lower, mid, and upper orogenic crust in the Grenville Province—Implications for the evolution of large hot long-duration orogens. *Precambrian Res.* **2008**, *167*, 237–259. [CrossRef]
17. Selleck, B.W.; McLelland, J.M.; Bickford, M.E. Granite emplacement during tectonic exhumation: The Adirondack example. *Geology* **2005**, *33*, 781. [CrossRef]
18. Wong, M.S.; Williams, M.L.; McLelland, J.M.; Jercinovik, M.J.; Kowalkoski, J. Late Ottawan extension in the eastern Adirondack Highlands: Evidence from structural studies and zircon and monazite geochronology. *Geol. Soc. Am. Bull.* **2011**, *124*, 857–869. [CrossRef]
19. McLelland, J.; Hamilton, M.; Selleck, B.; McLelland, J.M.; Walker, D.; Orrell, S. Zircon U- Pb geochronology of the Ottawan orogeny, Adirondack Highlands, New York. Regional and tectonic implications. *Precambrian Res.* **2001**, *109*, 39–72. [CrossRef]
20. Valley, P.M.; Hanchar, J.M.; Whitehouse, M.J. Direct dating of Fe oxide-(Cu-Au) mineralization by U/Pb zircon geochronology. *Geology* **2009**, *37*, 223–226. [CrossRef]
21. Postel, A.W. *Geology of the Clinton County Magnetite District, New York*; US Geological Survey: Reston, VA, USA, 1952; Volume 237, p. 95.
22. Geer, P.S.; Regan, S.P.; Walsh, G.J.; Williams, M.L.; Lupulescu, M.V.; Valley, P.M. Multiple stages of mineralization of the hammondville magnetite-apatite deposits. In Proceedings of the Northeast Geological Society of America Annual Meeting, Mount Washington, NH, USA, 21–23 March 2016.
23. Knipping, J.L.; Bilenker, L.D.; Simon, A.C.; Reich, M.; Barra, F.; Deditius, A.P.; Lundstrom, C.; Bindeman, I.; Munizaga, R. Giant Kiruna-type deposits form by efficient flotation of magmatic magnetite suspensions. *Geology* **2015**, *43*, 591–594. [CrossRef]

24. Lupulescu, M. Minerals from the Iron Deposits of New York State. *Rocks Mineral.* **2008**, *83*, 248–266. [CrossRef]
25. Hill, B.M.; Clechenko, C.C.; Valley, J.W.; Hamilton, M.A.; McLelland, J.M.; Bickford, M.E. Direct dating of Adirondack massif anorthosite by U-Pb SHRIMP analysis of igneous zircon: Implications for AMCG complexes. *Geol. Soc. Am. Bull.* **2004**, *116*, 1299–1317.
26. Regan, S.P.; Chiarenzelli, J.R.; McLelland, J.M.; Cousens, B.L. Evidence for an enriched asthenospheric source for coronitic metagabbros in the Adirondack Highlands. *Geosphere* **2011**, *7*, 694–709. [CrossRef]
27. Lupulescu, M.V.; Chiarenzelli, J.R.; Bailey, D.G.; Regan, S.P. The magnetite-fluorapatite ores from the eastern Adirondacks, New York: Cheever Mine. In Proceedings of the New York State Geological Association Annual Meeting, Plattsburgh, NY, USA, 12–13 September 2015.
28. Regan, S.P.; Walsh, G.J.; Williams, M.L.; Chiarenzelli, J.R.; Toft, M.; McAleer, R. Syn-collisional exhumation of hot middle crust in the Adirondack Mountains: Implications for extensional orogenesis in the southern Grenville Province. *Geosphere* **2019**. under review.
29. Budzyń, B.; Harlov, D.E.; Williams, M.L.; Jercinovic, M.J. Experimental determination of stability relations between monazite, fluorapatite, allanite, and REE-epidote as a function of pressure, temperature, and fluid composition. *Am. Mineral.* **2011**, *96*, 1547–1567.
30. Budzyń, B.; Harlov, D.E.; Kozub-Budzyń, G.A.; Majka, J. Experimental constraints on the relative stabilities of the two systems monazite-(Ce)–allanite-(Ce)–Fluorapatite and xnotime-(Y)–(Y, HREE)-rich epidote–(Y,HREE)-rich fluorapatite, in high Ca and Na-Ca environments uner P-T conditions of 200–1000 MPa and 450–750 °C. *Contrib. Mineral. Petrol.* **2017**, *111*, 183–217.
31. Jercinovic, M.J.; Williams, M.L.; Lane, E.D. In-situ trace element analysis of monazite and other fine-grained accessory minerals by EPMA. *Chem. Geol.* **2008**, *254*, 197–215. [CrossRef]
32. Pouchou, J.L.; Pichoir, F. "PAP" phi-rho-Z procedure for improved quantitative microanalysis. In *Microbeam Analysis*; Armstrong, J.L., Ed.; San Francisco Press Inc.: San Francisco, CA, USA, 1985; pp. 104–106.
33. Allaz, J.; Williams, M.L.; Jercinovic, M.J.; Donovan, J. A new technique for electron microprobe trace element analysis: The multipoint background method. In Proceedings of the EMAS 2011, Modern Developments and Applications in Microbeam Analysis, Angers, France, 15–19 May 2011; pp. 319–320.
34. Dumond, F.; McLean, N.; Williams, M.L.; Jercinovic, M.J.; Bowring, S.A. High resolution dating of ranite petrogenesis and deformation in a lower crustal shear zone: Athabasca granulite terrane, western Canadian Shield. *Chem. Geol.* **2008**, *16*, 175–196. [CrossRef]
35. Vernon, R.H. *A Practical Guide to Rock Microstructure*; Cambridge University Press (CUP): Cambridge, MA, USA, 2004.
36. Harlov, D.E.; Forster, H.-J. Fluid-induced nucleation of (Y + REE) phosphate minerals within apatite: Nature and experiment. Part II. Fluorapatite. *Am. Mineral.* **2003**, *88*, 1209–1229. [CrossRef]
37. Betkowski, W.B.; Harlov, D.E.; Rakovan, J.F. Hydrothermal mineral replacement reactions for an apatite-monazite assemblage in alkali-rich fluids at 300–600 °C and 100 MPa. *Am. Mineral.* **2016**, *101*, 2620–2637. [CrossRef]
38. Harlov, D.E.; Wirth, R.; Förster, H.-J. An experimental study of dissolution–reprecipitation in fluorapatite: Fluid infiltration and the formation of monazite. *Contrib. Mineral. Petrol.* **2005**, *150*, 268–286. [CrossRef]
39. Harlov, D.E.; Wirth, R.; Hetherington, C.J. Fluid-mediated partial alteration in monazite: The role of coupled dissolution–reprecipitation in element redistribution and mass transfer. *Contrib. Mineral. Petrol.* **2010**, *162*, 329–348. [CrossRef]
40. Tropper, P.; Manning, C.E.; Harlov, D.E. Solubility of CePO4 monazite and YPO4 xenotime in H2O and H2O–NaCl at 800 °C and 1 GPa: Implications for REE and Y transport during high-grade metamorphism. *Chem. Geol.* **2011**, *282*, 58–66. [CrossRef]
41. Tropper, P.; Manning, C.E.; Harlov, D.E. Experimental determination of CePO4 and YPO4 solubilities in H2O-NaF at 800 °C and 1 GPa: Implications for rare earth element transport in high-grade metamorphic fluids. *Geofluids* **2013**, *13*, 372–380. [CrossRef]
42. Harlov, D.E.; Marschall, H.R.; Hanel, M. Fluorapatite-monazite relationships in granulite-facies metapelites, Schwarzwald, southwest Germany. *Mineral. Mag.* **2007**, *71*, 223–234. [CrossRef]
43. Schermaier, A.; Finger, F.; Broska, I.; Roberts, M.P. Replacement of primary monazite by apatite-allanite-epidote coronas in an amphibolite facies granite gneiss from the Eastern Alps. *Am. Mineral.* **1998**, *83*, 248–258.

44. Cherniak, D.; Watson, E.; Grove, M.; Harrison, T. Pb diffusion in monazite: A combined RBS/SIMS study. *Geochim. Cosmochim. Acta* **2004**, *68*, 829–840. [CrossRef]
45. Cherniak, D.; Pyle, J. Th diffusion in monazite. *Chem. Geol.* **2008**, *256*, 52–61. [CrossRef]
46. Seydoux-Guillaume, A.-M.; Paquette, J.-L.; Wiedenbeck, M.; Montel, J.-M.; Heinrich, W. Experimental resetting of the U–Th–Pb systems in monazite. *Chem. Geol.* **2002**, *191*, 165–181. [CrossRef]
47. Seydoux-Guillaume, A.-M.; Montel, J.-M.; Bingen, B.; Bosse, V.; De Parseval, P.; Paquette, J.-L.; Janots, E.; Wirth, R. Low-temperature alteration of monazite: Fluid mediated coupled dissolution–precipitation, irradiation damage, and disturbance of the U–Pb and Th–Pb chronometers. *Chem. Geol.* **2012**, *330*, 140–158. [CrossRef]
48. Allaz, J.; Selleck, B.; Williams, M.L.; Jercinovic, M.J. Microprobe analysis and dating of monazite from the Potsdam Formation, New York: A progressive record of chemical reaction and fluid interaction. *Am. Mineral.* **2013**, *98*, 1106–1119. [CrossRef]